

On the Unsteady Behavior of the Flow Around NACA 0012 Airfoil with Steady External Conditions at $Re=1000$

Dilek Funda Kurtulus

Aerospace Engineering Department METU 06800 Ankara, Turkey, dfunda@ae.metu.edu.tr

ABSTRACT

Even for the stationary airfoils, due to the boundary and shear layer interactions of upper and lower surface of the airfoils, alternating vortex patterns form and the flow becomes time dependent. In the current study, the unsteady behavior of the flow around a symmetric airfoil is considered as incidence angle increases. The flow patterns are presented for wide range of angles of attack values. The vortex pattern generated is analyzed numerically for different angles of attack at $Re=1000$ around NACA 0012 airfoil. At this Reynolds number, the flow is laminar and boundary layers are quite thick. Flow separation and unsteady vortex shedding is observed even at low angles of attack. For NACA 0012 airfoil, the unsteady vortex pattern is observed at about 8° angle of attack for $Re=1000$. Spectral analysis is performed for angles of attack ranging from 0° to 90° . It is presented that amplitude spectrum of lift coefficient (C_l) start to shows a peak at 8° for NACA 0012 and the aerodynamic forces presents oscillatory behavior afterwards. The effect of angle of attack to wake pattern and instantaneous and mean aerodynamic coefficients are discussed. The time-averaged streamlines, pressure and skin friction coefficients are analyzed to observe the vortex formation and separation from the airfoil upper surface at this low Reynolds number.

1. INTRODUCTION

Most of the insects fly at Reynolds number of 10^3 - 10^4 and most of the birds fly at Reynolds number of 10^4 to 10^5 due to their low speed and small length scales [1, 2]. The Reynolds number for species such as hummingbirds is $Re = O(10^4)$, while for smaller insects, such as fruit flies or honeybees, $Re = O(10^2 - 10^3)$ [3]. Flapping wing Micro Air Vehicles (MAVs), which are imitating flights of birds and insects, have favorable designs for low Reynolds number regime compared to fixed wing MAVs. For the design and control purpose of MAVs, the understanding of unsteady phenomena of low Reynolds numbers flows becomes important in last decades [4-6].

The knowledge of unsteady behavior of airfoils at low Reynolds numbers with steady external conditions will also increase the knowledge of vortex shedding phenomena of flapping airfoils in this flight regime. The analytical models defined for these flapping motions are most of the time based on the quasi-steady approaches [7]. In order to understand physical characteristics of a wing in unsteady motion, it is important to have fundamental knowledge as well on steady condition. C_l - α , C_l - C_d relations can be used to understand perching, flapping (plunging/pitching) airfoils by considering effective angle of attack [6].

Ohmi et al. [8-9] have studied both experimentally and numerically vortex formation around an ellipse and a NACA 0012 airfoil oscillating and translating at $Re=1500$ to 10000 . The experiments are carried out in a water tank. The wake patterns are classified according to the shedding and development of vortices as static stall type (being similar to the vortex pattern of a high incidence fixed airfoil), synchronized shedding type (where leading edge vortices are combined into the co-rotating trailing edge vortices and then shed downstream in a synchronized way), parallel shedding type (where both leading edge and trailing edge vortices are shed downstream with trailing edge generating its own alternating vortices) and vortex superposition type (where leading edge vortices generated superposed on each other to form a single standing vortex and then detach from the airfoil). By using the same experimental water tank of Ohmi et al. [9], with a modified traverse and rotational mechanisms,

Kurtulus et al. [7, 10] have investigated experimentally flow physics around pitching/plunging NACA 0012 airfoil at $Re=1000$.

Currently in literature, some focus is also given to perching maneuvers at low Reynolds number [11, 12]. The perching maneuver is similar to pitch-up problem, where the angle of attack varies over a large amplitude [11]. Ol et al. [11] studied at constant pitch rate the flow around flat plate and 10% thick ellipse at $Re=100$ and $Re=1000$ at an amplitude ranging from 0° to 40° . The understanding of the flow physics at steady conditions will also increase the knowledge about micro air vehicle applications including perching, gust response, maneuvering flight and flapping wings in order to control these MAVs and model the system.

Wakes behind high angle of attack airfoils and bluff bodies are unsteady under most conditions even at steady external conditions. It is important to understand the physics of flow separation and vortex formation [13]. With low Reynolds number aerodynamics, the flow is laminar and prone to separate even under a mild adverse pressure gradient. It should be also noted that the development of coherent structures in the airfoil wake at low Reynolds numbers is of interest also due to structural vibrations and noise generation [14]. Aerodynamics of airfoils operated at low Reynolds numbers has recently also gained an importance for small wind turbine applications. In addition, previous works on low Reynolds numbers have paid little attention to the flowfield and aerodynamic properties at large angle of attack [15].

There are very few analysis in literature on unsteadiness of flows around airfoils at low Reynolds numbers of order 10^3 with steady free-stream. The flow at these Re numbers is highly nonlinear and complex viscous phenomena are present.

Different numerical simulations are carried out in steady external conditions by researchers for $Re=O(10^2-10^4)$ but mainly for low angles of attack ranges.

From Stanford University, Kunz and Kroo [16] use a two-dimensional incompressible Navier-Stokes solver INS2D which utilizes the artificial compressibility method. Analysis were done at angles of attack lower than about 10° with Reynolds number ranging from 1000 to 12000 for different thickness (from 2% to 10 %) and cambered NACA profiles.

Mateescu and Abdo [17] used a pseudo-time integration method using artificial compressibility to accurately solve the Navier-Stokes equations for Reynolds number ranging from 400 to 6000 at low angles of attack. Their results are very close to Kunz and Kroo [16] solutions.

Ahuja and Rowley [18] have performed a study on a flat plate at $Re=100$ for angles of attack ranging from 0° to 90° and proposed an estimator-based control design procedure using reduced-order models for flow control of unstable linear systems. They revealed a transition from a stable equilibrium to periodic vortex shedding as the angle of attack is increased beyond a critical value of $\alpha=27^\circ$ for $Re=100$. They have compared the maximum, minimum and mean aerodynamic forces and generated vortex fields at different angles of attack.

Based on their DNS data, Hoarau et al. [19] calculated the lift and drag coefficients of NACA0012 airfoil at $\alpha=20^\circ$ for different Reynolds numbers of $8 \times 10^2-1 \times 10^4$. Hoarau et al. [20] showed that two types of organized modes appears namely von Karman mode for Re below 2000 and shear layer mode for Reynolds numbers bigger than equal to 2000.

Gopinath et al. [13] investigated NACA 0012 airfoil at $\alpha=20^\circ$ and $Re=1000$ with their time spectral approach where they propose a method to compute the time period as part of the solution to the unsteady problem, in cases where the frequency of unsteadiness is not predefined. Mittal [21] have performed finite element computation of incompressible flow around NACA 0012 airfoil at $Re=10^3$ and $Re=5 \times 10^3$ for $\alpha=10^\circ$. Liu et al. [22] have used finite element method combined with Arbitrary-Lagrangian-Eulerian (ALE) frame and explicit Characteristic Based Split Scheme (CBS) to study numerically flows around static and pitching airfoils. They analyzed NACA 0012 static airfoil at $Re=10^3$ for angles of attack less than 30° .

Khalid et al. [23] performed CFD simulations using ANSYS Fluent software and compared their results with Liu et al. [22] solutions. They concluded that the steady state temporal solutions for lift and drag contain both odd and even harmonics which indicate the presence of quadratic as well as cubic nonlinearity in the system. They observed periodic doubling at $\alpha=22^\circ$ which leads to chaos at $\alpha=27^\circ$. Suzuki et al. [24, 25] developed a hybrid unsteady-flow simulation technique combining direct numerical simulation (DNS) and particle tracking velocimetry (PTV) and investigated flows past NACA 0012 airfoil at $\alpha=15^\circ$ for $Re=1000$ and 1300, then up to $Re=10^4$. Huang et al. [26] conducted an experiment in a water tank using particle tracking flow visualization and particle image velocimetry

(PIV) methods to analyze vortex evolution on the suction surface of an impulsively starting NACA 0012 wing. Five characteristic vortex evolution regimes are identified depending on the angle of attack and Reynolds number, namely attached flow, trailing edge vortex, separation vortex, leading edge vortex and bluff body effect.

Particle image velocimetry (PIV), laser-doppler anemometry (LDA), and laser-induced fluorescence (LIF) flow visualization measurements were performed around NACA 0012 airfoil in a water tunnel by Mahbub Alam et al. [15]. The work aims to study the near wake of the airfoil and its dependence on Re and α in the range of $Re = 5.3 \times 10^3 - 5.1 \times 10^4$ and $\alpha = 0^\circ - 90^\circ$.

Reynolds number effects play a dominant role in the aerodynamics of MAVs and small UAVs. As the Reynolds number decreases, the overall performance of a lifting body decreases. The recent interest in the development of flapping wing micro air vehicles has revealed a need for a more thorough understanding of the aerodynamics of airfoils at low speeds. In response to this need, a study of the lift, drag, and pitching moment characteristics of NACA 0012 airfoil at low Reynolds number of 1000 are presented for angles of attack in the range of $0^\circ - 90^\circ$ using a finite-volume based package program ANSYS Fluent [27].

The flow structure analysis includes the unsteady and time averaged vortex formation and their effects on aerodynamic coefficients. The current results are presented to describe the vortex shedding phenomena at low speed and small length scales for wide range of angles of attack. Analysis of the data includes comparison of instantaneous and mean aerodynamic forces, mean lift-curve slope, mean streamline patterns, transition location and Strouhal number.

2. NUMERICAL METHOD

2.1 Governing equations and geometry

The governing equations are Navier-Stokes equations for incompressible, laminar and two dimensional flow:

$$\vec{\nabla} \cdot \vec{V} = 0 \quad (1)$$

$$\frac{\partial \vec{V}}{\partial t} + (\vec{V} \cdot \vec{\nabla}) \vec{V} = -\frac{1}{\rho} \vec{\nabla} p + \nu \nabla^2 \vec{V} \quad (2)$$

where \vec{V} is the velocity vector, ρ is the fluid density, p is the pressure, ν is the kinematic viscosity. ANSYS Fluent implements the finite-volume method to solve conservation equations [27]. The pressure-velocity coupling is done by means of the SIMPLE-type fully implicit algorithm. Pressure-velocity coupling is used with a predictor-corrector pressure scheme. Transient solution has been approximated using second order implicit method. The solution is second-order accurate in space and time. The velocity inlet boundary condition is used at the semi-circular region of the outer domain and pressure outlet is used at the other side of the outer region.

The flow around NACA 0012 airfoil is obtained at $Re=1000$ steady external conditions. The thickness distribution of NACA 4 digit airfoils, y_t , is found by using Eq. 3 [28, 29].

$$y_t = \pm \frac{t/c}{0.2} \cdot (0.2969 \cdot \sqrt{x} - 0.1260 \cdot x - 0.3516 \cdot x^2 + 0.2843 \cdot x^3 - 0.1015 \cdot x^4) \quad (3)$$

where $x \in [0, 1]$ and t/c is the maximum thickness to chord ratio, which is in percentage last two digits of NACA 4 digit airfoils. The far field boundary is located at $15c$ away from the airfoil. NACA 0012 airfoil is a symmetric airfoil so the thickness distribution is sufficient for the upper and lower surface definitions.

The angle of attack, defined to be positive in the clockwise direction was varied from 0 to 90° with an increment step of 1° for $\alpha < 41^\circ$ and 10° for $40^\circ < \alpha < 90^\circ$. The pivot point was at the quarter chord location ($0.25c$) from the leading edge of the NACA 0012 airfoil. It should be noted that pitching moment calculations are performed with respect to this pivot point for the current study.

2.2 Grid and time refinement studies

Detailed grid and time refinement studies are carried out for two different angles of attack, namely 10° and 20° . To perform grid refinement studies 3 different meshes are used. A preprocessor is created with MATLAB program to form a journal file for GAMBIT grid generation software so that the boundary shapes and number of nodes and elements can be adjusted for all cases with an almost equal accuracy (numbers of elements, nodal points...). The coarse mesh consists of 150 nodes, medium mesh 300 nodes and fine mesh 500 nodes around the airfoil. Total number of elements in the domain are given in Table 1. The first cell spacing of the boundary layer has value of $0.002c$ for coarse and medium meshes and $0.0015c$ for fine mesh. The mesh around the airfoil is composed of two parts, namely inner region and outer region. The inner region above the boundary layer is constructed with a semi-circle having radius of $1.5c$ centered at the airfoil $c/4$ location at the upstream and a rectangular region with width of $1.5c$ at the downstream of the airfoil. The inner region mesh is unstructured triangular grid. The outer domain is of C-type structured mesh with $15c$ radius (Figure 1). With the preprocessor program the airfoil is rotated for the given angle of attack in the inner region by keeping the outer domain and wake region fixed with the same structured grid. Grid refinement study is carried out with time increment of $\Delta t=0.005s$. The results are simulated until $t=100s$ which corresponds to a non-dimensional time of $t^*=t.U_{inf}/c=146$ where $U_{inf}=0.146\text{ m/s}$ is the free stream velocity and $c=0.01\text{ m}$ is the chord length of the airfoil. The computational time interval is $t^* \in [0\ 146]$. It should be noted that in the current paper, the start-up problem is used as an initial condition for starting the computations, and the paper is concerned with the solutions after relaxation to steady state or periodic conditions.

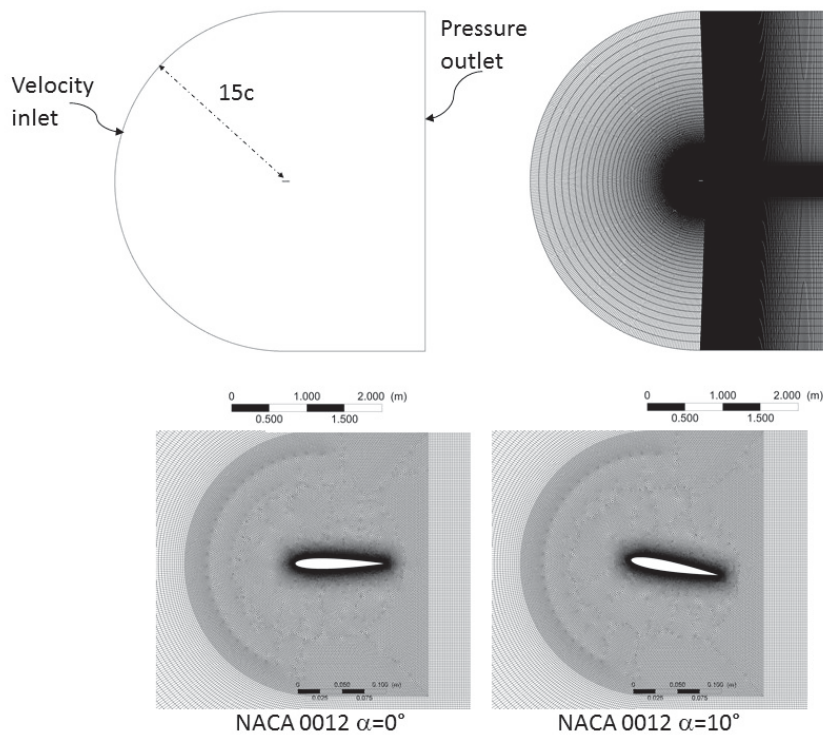


Figure 1. Computational domain for medium mesh

Table 1. Computational mesh for NACA 0012 airfoil at $\alpha=10^\circ$ and $\alpha=20^\circ$

Domain	Nodes around airfoil	Total number of Elements
Coarse mesh	150	93915
Medium mesh	300	194961
Fine mesh	500	248168

From the grid refinement study, it is concluded that the initial start region results almost same aerodynamic coefficients for all three meshes. However, after $t^*=12.4$, coarse mesh results deviate slightly from medium and fine mesh solutions and a phase shift occurs throughout the following cycles. The remaining results are obtained with medium mesh since the difference between fine mesh and medium mesh in terms of mean aerodynamic forces is less than 0.5 %.

For $\alpha=20^\circ$, coarse mesh results a phase difference when compared with medium and fine meshes. However, in this case the deviation starts earlier at time $t^*=6.2$. Its influence is more visible at later time instances compared to $\alpha=10^\circ$ case.

Similarly a time refinement study is carried out with the medium mesh for time increments (Δt) of 0.01s, 0.005s and 0.0025s. A small phase shift is observed with $\Delta t=0.01$ s compared to other two solutions. It is observed that the results for $\Delta t=0.005$ s and 0.0025s are very close to each other. The rest of the study is performed with time increment of $\Delta t=0.005$ s.

The results for grid and time refinement studies are represented for time intervals of $t^* \in [0 \ 30]$ and $t^* \in [73 \ 80]$ at $\alpha=10^\circ$ and $\alpha=20^\circ$ in Figure 2 and Figure 3 respectively. It should be noted that in the current study C_l , C_d and C_m denotes the lift, drag and moment coefficients for the airfoil, respectively. The corresponding mean values are calculated in the interval of $t^* \in [73 \ 146]$ and denoted with \bar{C}_l , \bar{C}_d , and \bar{C}_m .

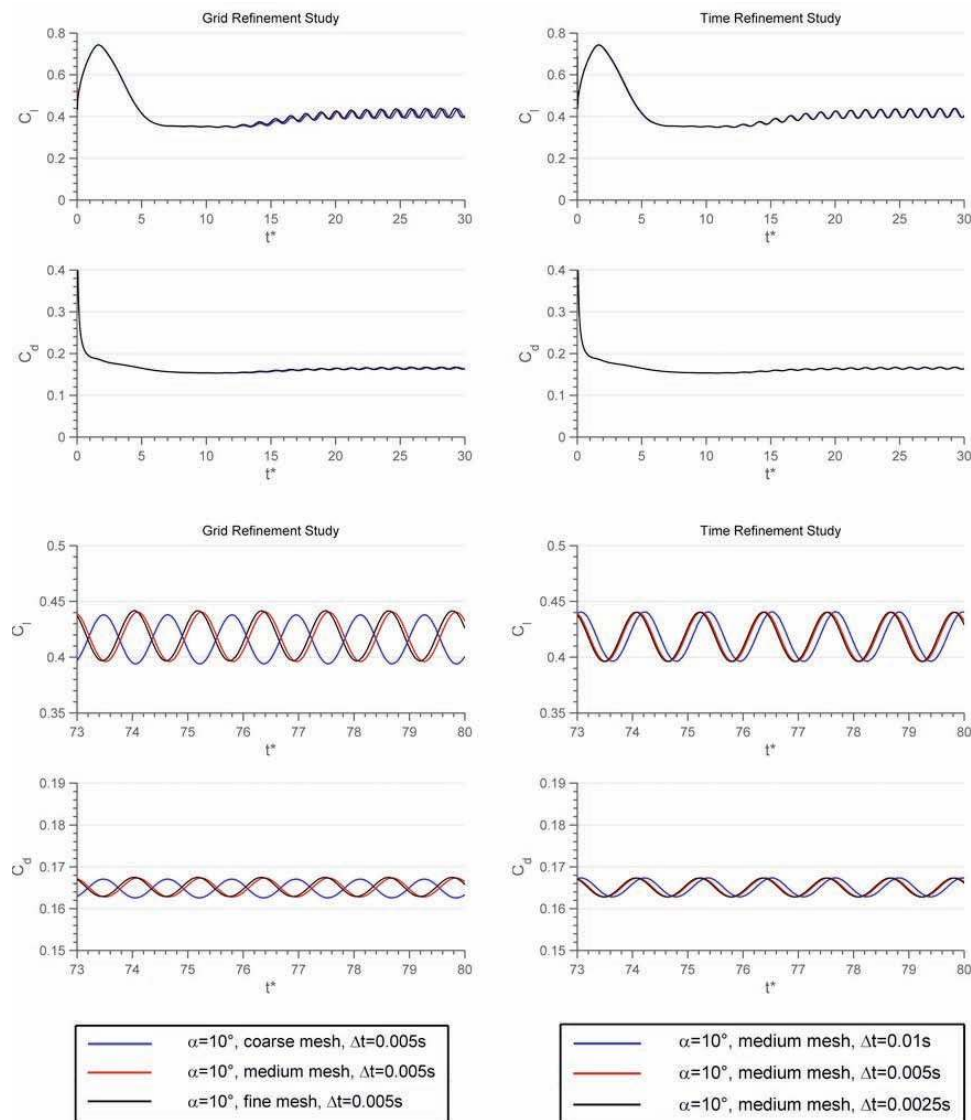


Figure 2. Grid (left column) and time (right column) refinement studies at $t^* \in [0 \ 30]$ and at $t^* \in [73 \ 80]$ for $\alpha=10^\circ$

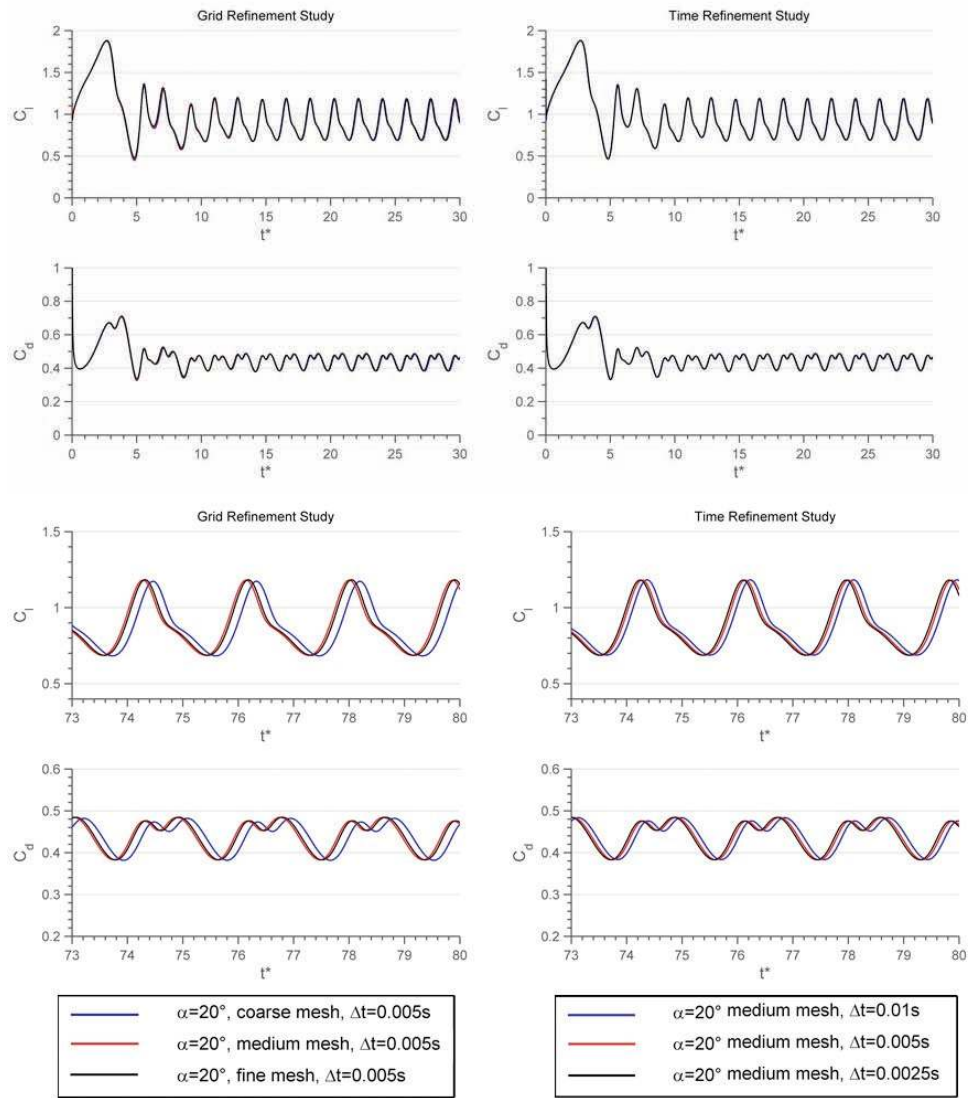


Figure 3. Grid (left column) and time (right column) refinement studies at $t^* \in [0, 30]$ and at $t^* \in [73, 80]$ for $\alpha=20^\circ$

3. RESULTS

The solutions for different angles of attack are obtained from $\alpha=0^\circ$ to $\alpha=90^\circ$. The results are obtained with 1° increments from $\alpha=0^\circ$ to $\alpha=41^\circ$ and with 10° increments from $\alpha=40^\circ$ until 90° . The aim of the present study is to investigate creation of the unsteadiness due to vortex shedding at $Re=1000$. The unsteadiness is created at steady external conditions with fixed incidence angle.

3.1 Mean aerodynamic coefficients

Figure 4 presents the mean lift coefficient (\bar{C}_l) distribution versus angle of attack for NACA 0012 airfoil along with some published data at $Re=1000$ calculated by Mittal et al. (1994) at $\alpha=10^\circ$, Suziki et al. (2009) at $\alpha=15^\circ$, Hoarau et al. (2003) at $\alpha=20^\circ$, and Liu et al. (2012) and Khalid et al. (2012) for $\alpha < 30^\circ$. Their results are very close to present solution. In general, present data agrees with their simulations, thus providing a validation for the current calculations. The mean values for the current study are obtained in the time interval of $t^* \in [73, 146]$ in order not to take into account initial computational effects of the results. The minimum and maximum peak locations of the oscillations in this time interval are also presented in Figure 4a with bars in addition to the mean values (shown as black circles). The lift coefficient oscillates between these two peak locations during the time interval of $t^* \in [73, 146]$.

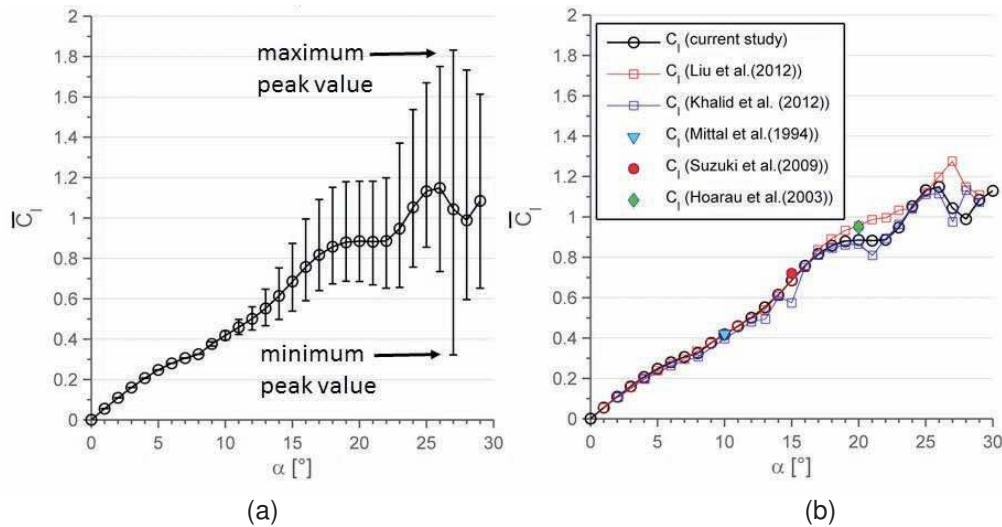
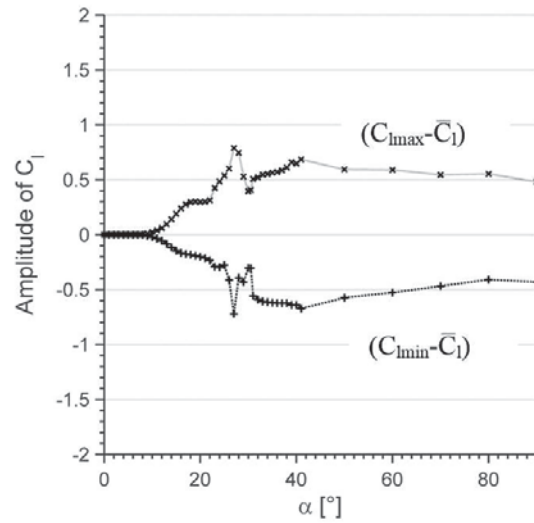


Figure 4. Mean lift coefficient \bar{C}_l and comparison with literature data at $Re=1000$

The stall of an airfoil is characterized by a rapid drop in the lift coefficient for a small increase in α . For low Reynolds numbers of order 1000, this drop is not observed rapidly but gradually in the mean value.

The initial alternating vortex shedding angle of attack is one of the critical angle of attack where oscillations in aerodynamic coefficients starts. This angle is 8° for NACA 0012 airfoil. \bar{C}_l become almost constant at about $\alpha=19^\circ$ - 21° where $\bar{C}_{l\alpha}$ is almost zero (Figure 6). Stall angle is observed to be at about $\alpha=26^\circ$ by considering mean values of the lift coefficients. Figure 4a shows the minimum and maximum amplitude values of the lift coefficient as error bars on the mean values. After 8° , this amplitude is observed to increase with increasing angle of attack until 27° . Figure 5 also shows the amplitude of C_l by presenting $(C_{lmax}-\bar{C}_l)$ and (\bar{C}_l-C_{lmin}) for $\alpha=0^\circ$ - 90° . The amplitude of C_l is zero until 8° , it increases until 27° and afterwards decreases until 30° . Then, from 31° to 41° , an increase in the amplitude of the lift coefficient oscillation is observed. From 50° to 90° , the amplitude of lift coefficient slightly decreases. Beyond the stall angle of attack, mean \bar{C}_l displays a maximum value at around $\alpha=40^\circ$. It is also noted that the lift curve slope $\bar{C}_{l\alpha}$ is equal to π at $\alpha=0^\circ$ which is half of the linearized lift curve slope of 2π . Then, the curve slope decreases until $\alpha=8^\circ$ where a sudden increase of lift curve slope is observed afterwards (Figure 6). This figure shows why linear theories cannot be also used for low Reynolds number cases and correction factors are needed for lift curve slope calculations. It should also be noted that the curve slope is increasing with the decrease of the thickness of the airfoil as is can be seen also from the results of Kunz and Kroo [16] at low angles of attack. It should be also noted that, $C_{m\alpha}$ negative slope imply that NACA 0012 is statically stable around $\alpha=0^\circ$.

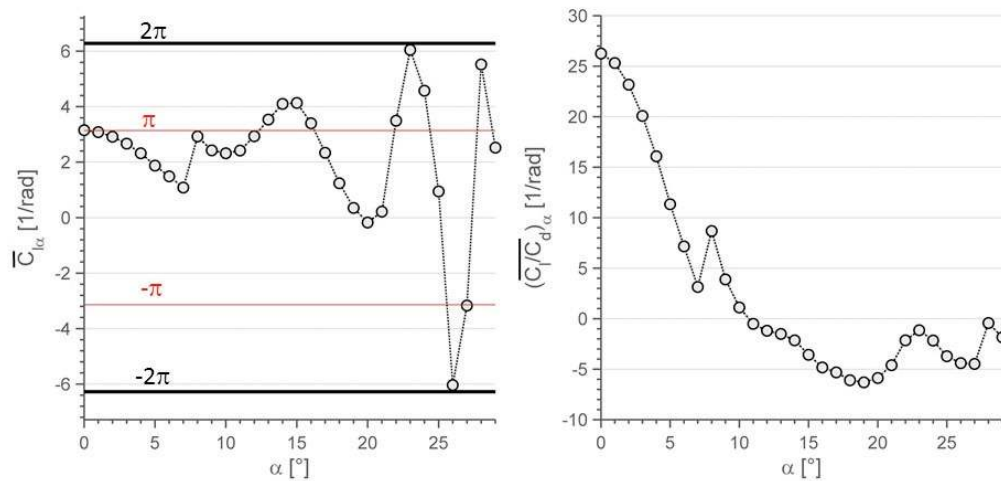
Figure 7 shows mean aerodynamic coefficients and their oscillation amplitudes for $\alpha=0^\circ$ - 90° . As can be seen from Figure 7, mean (C_l/C_d) increases from 0° until it reaches a maximum value of 2.55 at 11° angle of attack. Drag coefficient and zero angle of attack is found to be about 0.12 for NACA 0012 airfoil at $Re=1000$. It is observed that the mean drag coefficient increases as angle of attack increases (Figure 7) until an inflection point at about $\alpha=26^\circ$. At this point the drag coefficient is about $\bar{C}_d=0.69$. Afterwards, the mean drag coefficient decreases slightly until $\alpha=28^\circ$ to about 0.66 then the increasing trend of drag continue until $\alpha=90^\circ$ to a value of about 2.8 with a standard deviation of 0.3. It is observed that the amplitude spectrum of $\alpha=27^\circ$ reveals a dense spectrum of frequencies (see Figure 22a) as is also observed by Khalid et al. [23]. They have observed periodic doubling at $\alpha=22^\circ$ which leads to chaos at $\alpha=27^\circ$ [23]. It is also observed that the maximum amplitude of C_l is obtained at $\alpha=27^\circ$ as can be also seen from Figure 5. At $\alpha=29^\circ$, the amplitude spectrum of C_l becomes smooth and vortex shedding pattern turns out to be more ordered.

Figure 5: Amplitude of C_l

It should also be emphasized that about 56% increase in mean drag coefficient is observed between 30.5° - 31° . A run is also carried out at 30.5° to understand the effect of this jump. It is understood that a change of 0.5° will result in a vortex and wake pattern change (see Figure 9 and Figure 22b), an increase in the wake width and consequently resulting in sudden jumps in aerodynamic coefficients.

This increase is also observed in the mean lift coefficient as about 61 % and more dominantly about 120% in the mean pitching moment coefficient about the quarter chord location (Figure 7).

It should be noted that this jump is not due to the grid or time since the finest grid condition and finest time increment in this study are also applied to angles of attack of 35° and 40° to check grid and time independency even at high angles of attack. The medium and fine mesh results are very similar as in the case of 10° and 20° refinement solutions.

Figure 6: Slope curves of mean \bar{C}_l and mean (C_l/C_d)

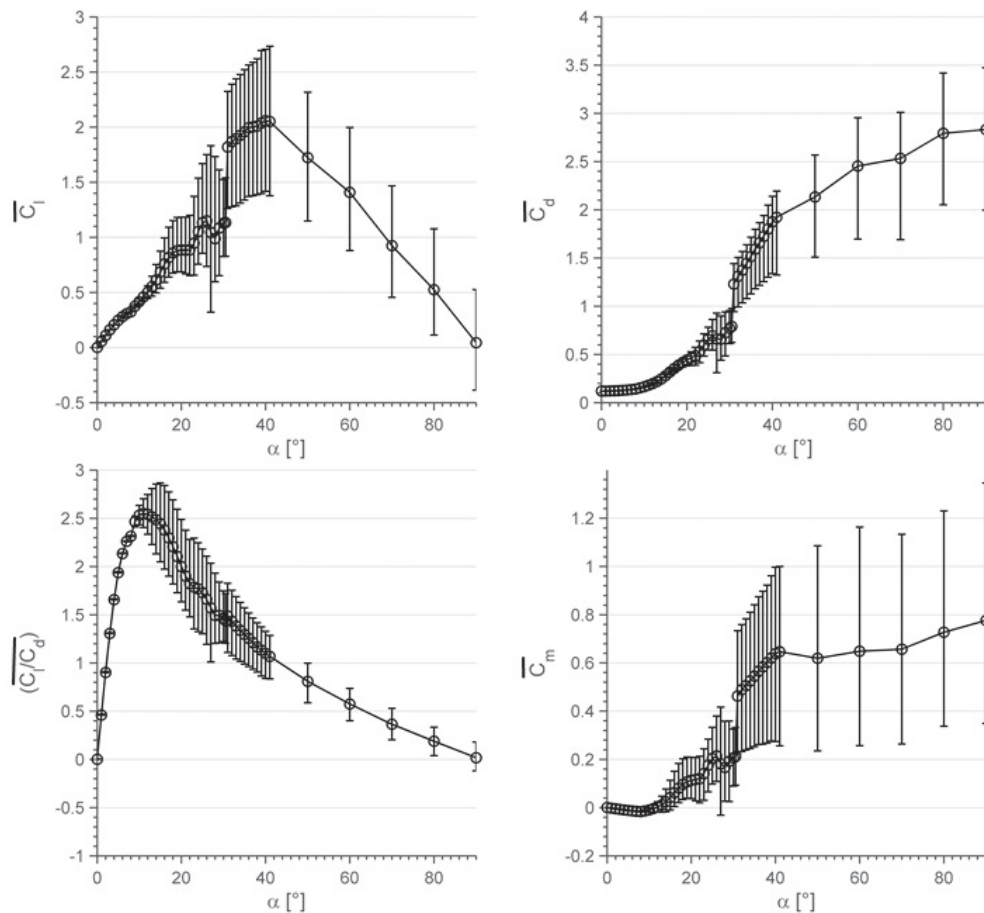


Figure 7. Mean aerodynamic coefficients for NACA 0012 at $Re=1000$ for different angles of attack

3.2 Mean and Unsteady vortex pattern

Karman vortex street theory characterizes the important feature of flow past bluff bodies, that is, the phenomenon of periodic vortex shedding. The vortex structure formed in the flowfield of an airfoil depends on angle of attack. Below 7° , no alternating vortices are observed on the airfoil and at the wake of the airfoil. The Karman vortex structure is observed at the wake of the airfoil at about $\alpha = 8^\circ$ for NACA 0012. Figure 8 to Figure 10 show the time-averaged streamlines around the airfoil for angles of attack ranging from 0° to 90° . Two counter-rotating vortices are observed at the trailing edge of the airfoil as can be seen from the streamline patterns of $\alpha = 5^\circ$ (Figure 8) which are more clearly visible at higher angles of attack (see Figure 8, $\alpha = 6^\circ$ and $\alpha = 7^\circ$). The trailing edge vortex was also observed by Huang et al. [22] at $\alpha = 3^\circ - 8^\circ$, where the flow on the suction surface separated from the trailing edge, forming vortices.

The clockwise vortex covers the upper surface of the airfoil as angle of attack increases. It is found that the separation point moves from trailing edge towards the half of the chord ($0.5c$) on the upper surface of the airfoil starting from 0° until 7° . The separation point reaches $0.5c$ at $\alpha = 7^\circ$ as shown also from the mean skin friction distribution around the airfoil in Figure 11. The separation point moves toward the leading edge as angle of attack increases from 7° to 15° . The location of separation point on the upper surface of the airfoil is approximately $0.4c$ for $\alpha = 8^\circ$, $0.35c$ for $\alpha = 9^\circ$, $0.24c$ for $\alpha = 11^\circ$, $0.11c$ for $\alpha = 15^\circ$ and $0.07c$ for $\alpha = 19^\circ$ (Figure 11-Figure 15).

On the upper surface of the airfoil, new counter-clockwise vortex is observed to be generated approximately at $0.74c$ for angles of attack higher than 15° . The initial formation of this bubble can be observed from the time-averaged streamlines on Figure 8 (2nd column) and also from the mean skin friction coefficient distribution around the airfoil at $\alpha = 15^\circ$ where negative C_f values are coming closer to zero at about $0.74c$ (Figure 15). It is observed that this bubble is moving on the airfoil upper surface

towards the leading edge as angle of attack increases. For example, at $\alpha=19^\circ$, the flow separated at the leading edge of the airfoil (at $0.07c$) reattaches at 0.58 chord. The formation of the new counterclockwise bubble causes this reattachment just behind the mid-chord as can be also observed from the mean streamline patterns in Figure 8 ($\alpha=19^\circ$). The bubble length is approximately $0.13c$ and the second separation is observed at $0.71c$ location. The trailing edge vortex in counter-clockwise direction now causes once more the flow to attach at $0.9c$.

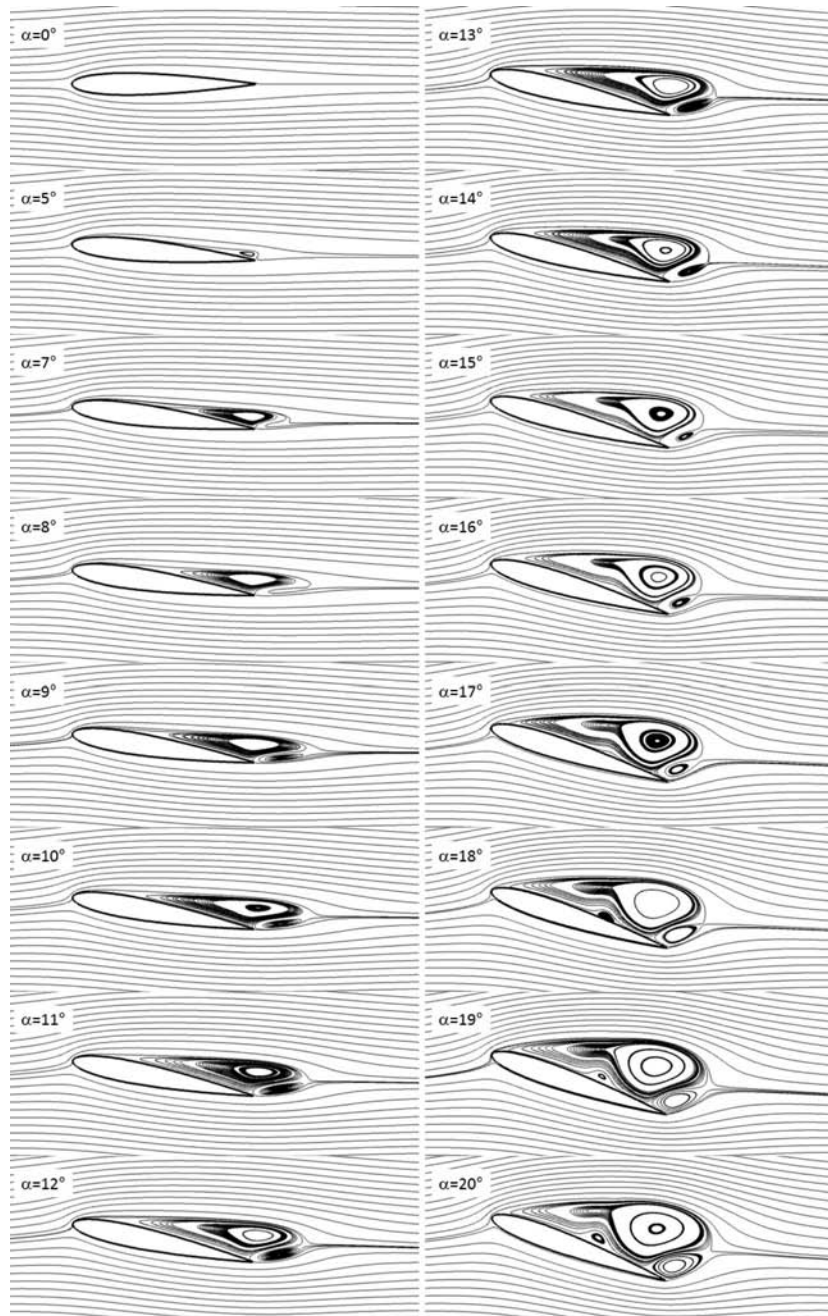


Figure 8. Streamlines of mean velocity field for angles of attack (α) below 20° (NACA 0012, $Re=1000$)

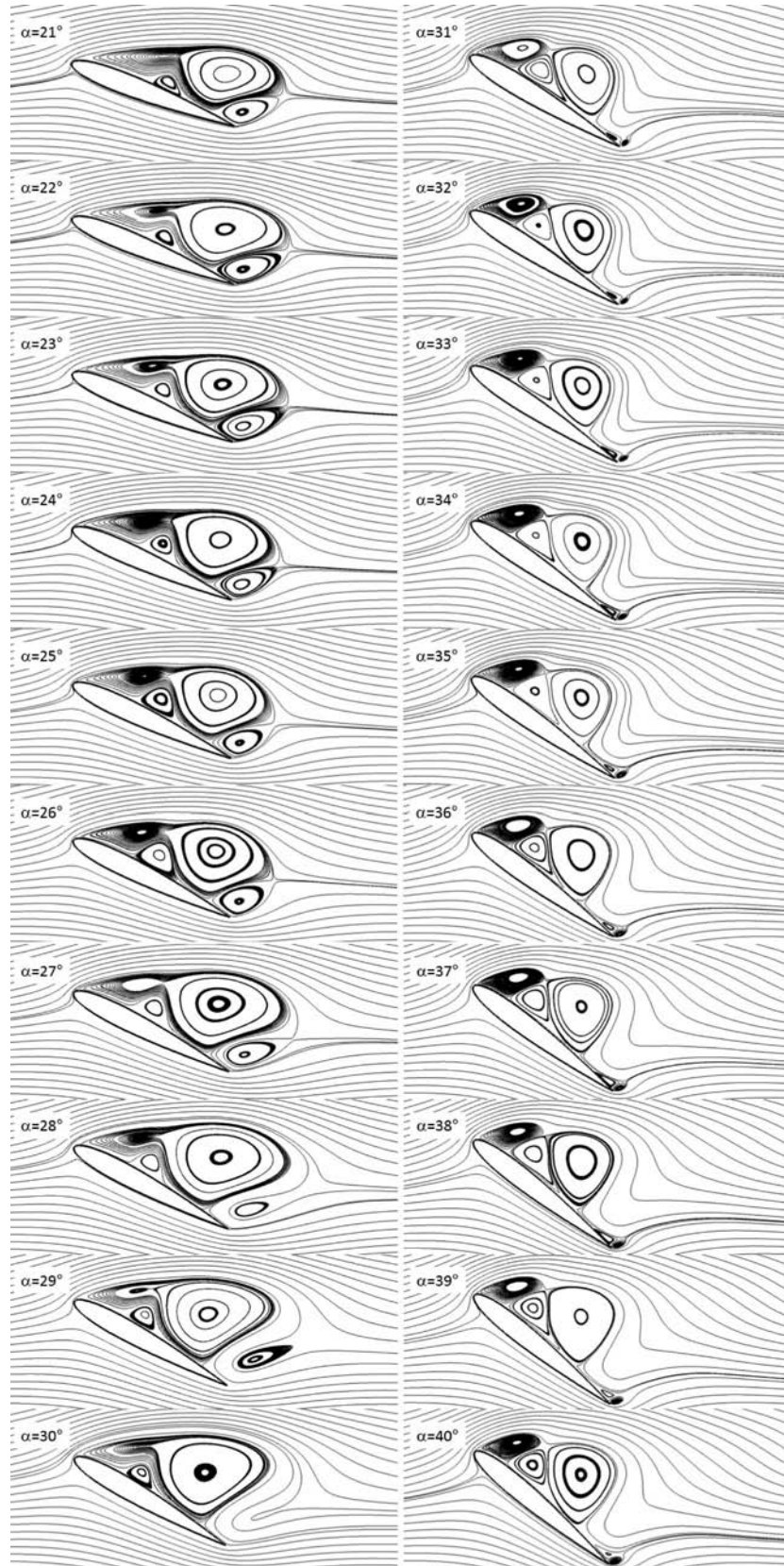


Figure 9. Streamlines of mean velocity field for angles of attack (α) between 21° and 40° (NACA 0012, $Re=1000$)

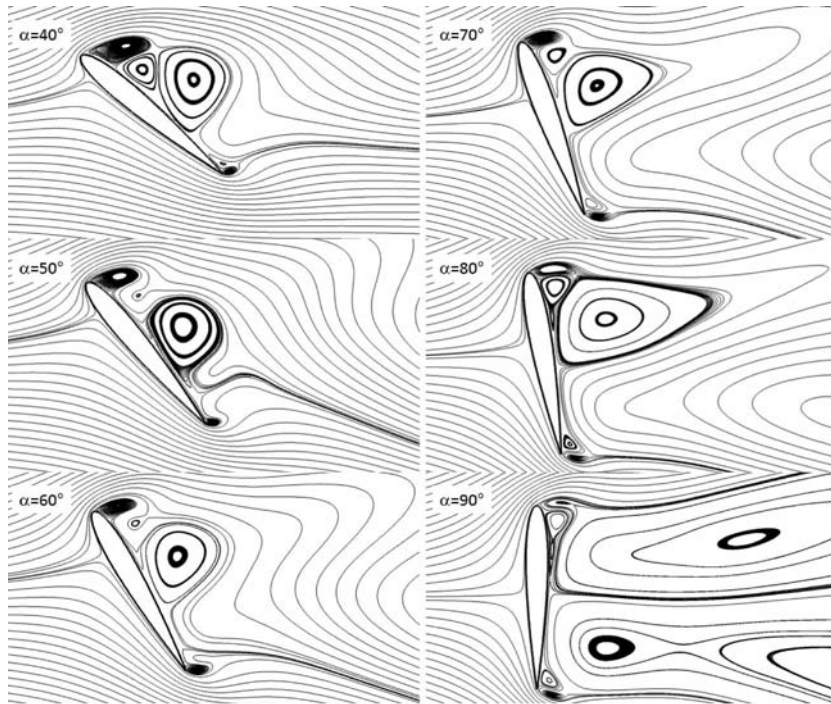


Figure 10. Streamlines of mean velocity field for angles of attack (α) between 40° and 90° (NACA 0012, $Re=1000$)

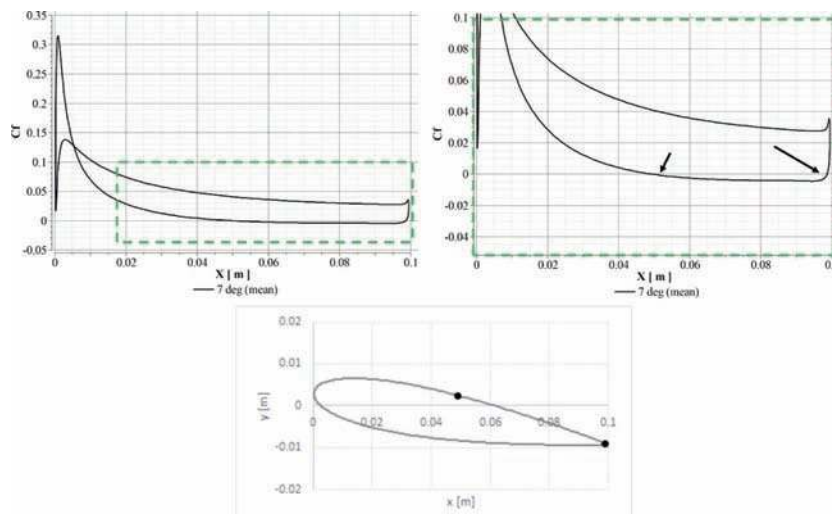
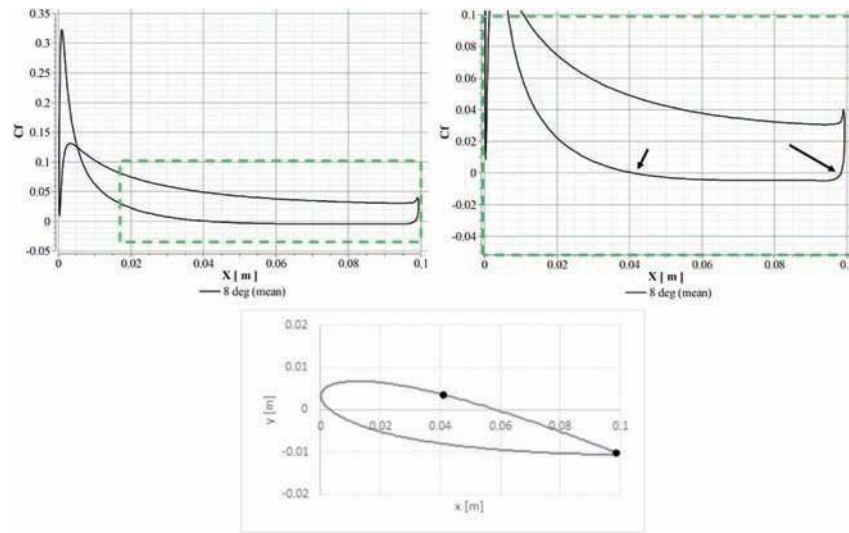
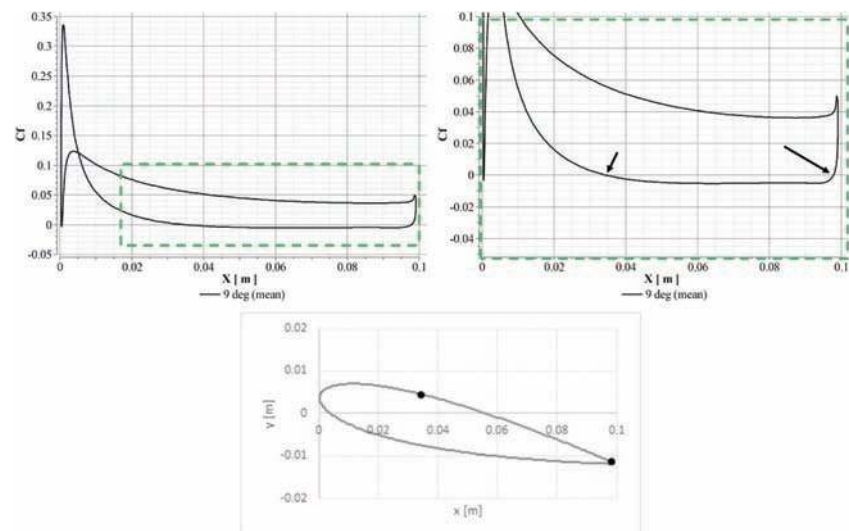
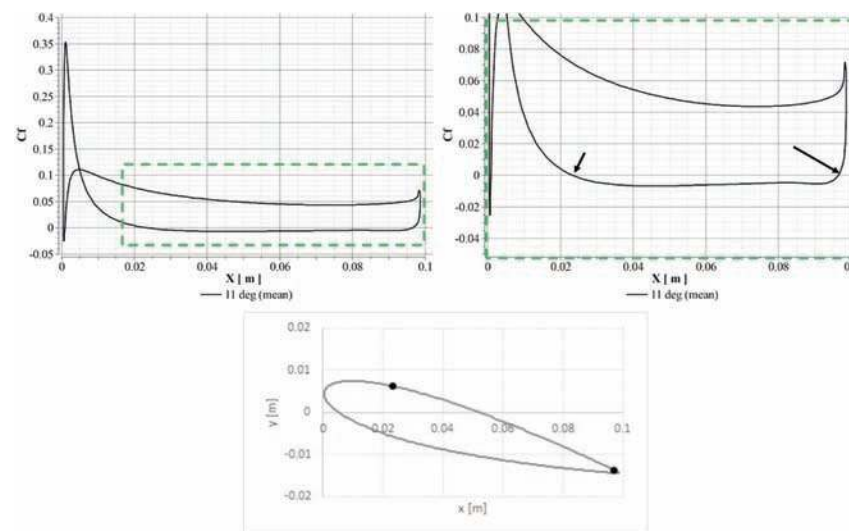
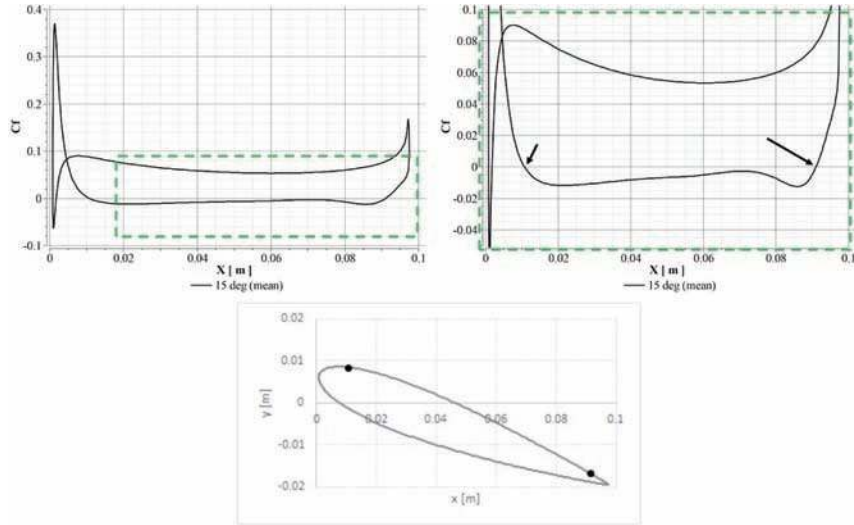
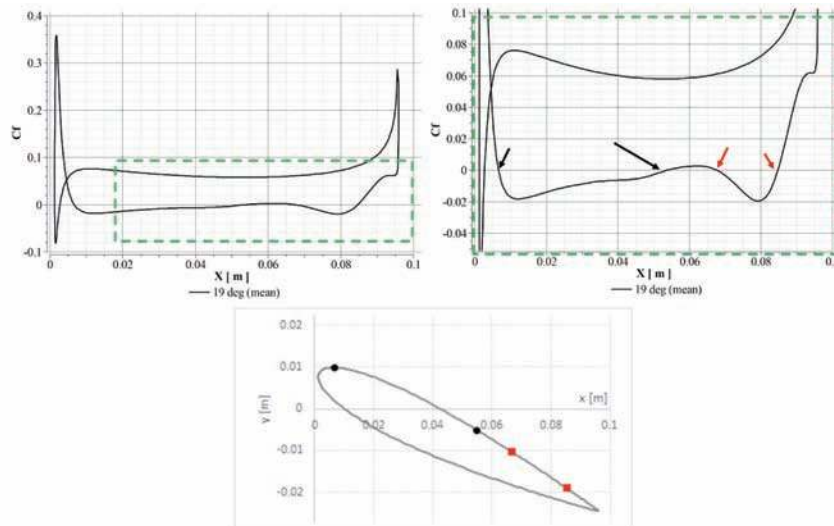


Figure 11. Mean skin friction coefficient and separation points on NACA 0012 at $\alpha=7^\circ$

Figure 12. Mean skin friction coefficient and separation point on NACA 0012 at $\alpha=8^\circ$ Figure 13. Mean skin friction coefficient and separation point on NACA 0012 at $\alpha=9^\circ$ Figure 14. Mean skin friction coefficient and separation points on NACA 0012 at $\alpha=11^\circ$

Figure 15. Mean skin friction coefficient and separation point on NACA 0012 at $\alpha=15^\circ$ Figure 16. Skin friction coefficient and separation points on NACA 0012 at $\alpha=19^\circ$

A comparison of time-averaged pressure coefficients around the airfoil are presented for angles between 7° - 19° in Figure 17. For $\alpha=9^\circ$, the mean pressure coefficient distribution increases in magnitude both on the upper surface and lower surface around the airfoil compared to $\alpha=8^\circ$ (Figure 17). As the separation point moves towards the leading edge from 7° to 19° , the leading edge suction pressure and trailing edge suction pressures on the upper surface is found to be increasing in magnitude.

Figure 18 shows the viscous drag (C_{dv}) and pressure drag (C_{dp}) effects of total mean drag coefficient at different angles of attack. It is observed that until 8° angle of attack viscous drag is the dominant term for the drag coefficient. At $\alpha=9^\circ$, both viscous drag and pressure drag coefficients are almost equal. A local maximum is also obtained at $\alpha=26^\circ$ at the pressure drag coefficient (as a result at the total drag coefficient). A sudden drag coefficient increase is also observed at $\alpha=31^\circ$. The vortex pattern between 30° and 31° shows an abrupt change in the vortex height as shown in Figure 9. Also, there is two new trailing edge vortices generated at $\alpha=31^\circ$. This vortex pattern results an abrupt change in pressure distribution and consequently increases the drag coefficient.

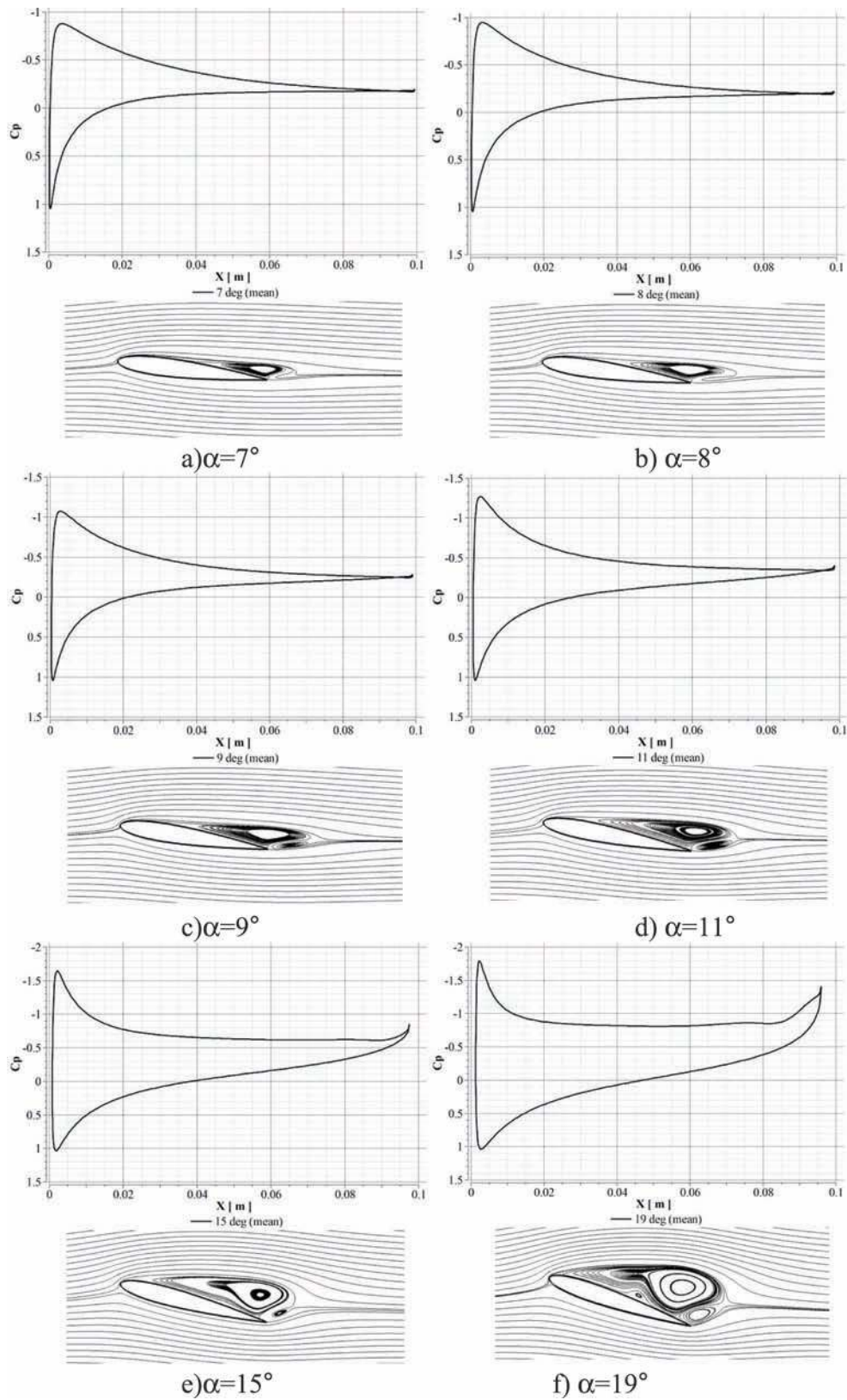


Figure 17. Mean pressure distribution around NACA 0012 at $\alpha=7^\circ$, 8° , 9° , 11° , 15° and 19°

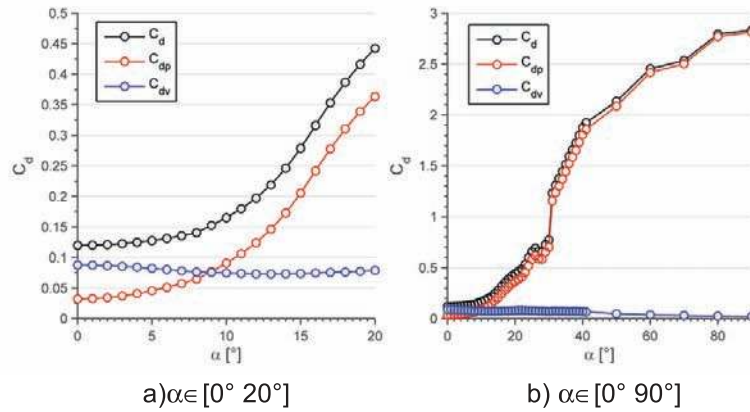


Figure 18. Mean viscous drag (C_{dv}), mean pressure drag (C_{dp}) and mean total drag ($C_d=C_{dv}+C_{dp}$) coefficients for NACA 0012 at different angles of attack

The unsteady aerodynamic coefficients and instantaneous vorticity distribution of NACA 0012 airfoil at $Re=1000$ are presented for $0^\circ < \alpha < 8^\circ$ in Figure 19. The analysis shows that the periodic behaviors of the aerodynamic coefficients are not observed for angles of attack below about 8° .

The two trailing edge vortices that are generated on the upper surface of the airfoil are not shed downstream of the airfoil for $0^\circ < \alpha \leq 7^\circ$. The aerodynamic coefficients are constant after the computational starting effects disappears (Figure 19-right column). The vortex shedding pattern is observed to be constant for angles of attack lower than 8° and alternating at the far downstream of the airfoil for $\alpha=8^\circ$ (Figure 19-left column). It should be noted that the same phenomena is observed in Ref. [9] for NACA 0012 airfoil at $Re=1000$ at $\alpha=8^\circ$, where it is stated that the unsteady vortex shedding initiates at this angle of attack. The two counter-rotating vortices generated at the trailing edge of the airfoil stays attached on the airfoil surface however the streamlines can be observed to be alternating up and down with time at the wake of the airfoil.

It is also interesting to note that, by Ahuja and Rowley [18] this critical angle of attack at $Re=100$ for a flat plate is found to be as 26° where periodic vortex shedding starts.

Huang et al. [26] observed five different flows, depending on angle of attack, ranging from 0° - 90° based on the flow visualization performed at $Re=1200$ - 2300 . The flow at $\alpha < 3^\circ$ corresponded to an attached flow, where the flow was completely attached on the entire upper surface of the airfoil. This result is also observed in the current study even with unsteady streamline patterns during the whole simulation period. Skin friction coefficient distribution on NACA 0012 below $\alpha=3^\circ$ do not show any separation point on the upper surface.

In the current study, the shedding phenomena is observed at the farfield of the airfoil at $\alpha=8^\circ$ which is similar to the results of Huang et al. [26]. They have also found that, $\alpha=8^\circ$ is also alternating vortex sheet formation angle even at slightly higher Reynolds numbers. The vortices form alternately above this angle of attack. Above 8° , the alternating vortices are observed just behind the airfoil. As angle of attack increases to the point where the flow separation is initiated, a shear layer forms near the separation point. The vortex created by this shear layer is in clockwise direction, however the vortex created by the shear layer formed from the trailing edge has a counterclockwise direction. These two shear layers roll up in opposite directions and an alternating wake rollup pattern is obtained [30].

It should be noted that these two shear layers formed on the upper and lower surface boundary layers are shown to be present at zero angle of attack at $Re=21000$ for a modified NACA 0012 airfoil as is explained in the flow visualization using hydrogen bubble technique by McAlister and Carr in 1978 [30, 31]. Their flow visualization experiments were performed in a water tunnel on a modified NACA 0012 airfoil and they compared steady state cases with airfoil at large amplitude harmonic oscillations in pitch.

Huang et al. [26] concluded that, at $\alpha=8$ - 17° , the boundary layer on the upper surface separated between the leading and trailing edges, forming vortices rolling on the surface, and eventually an alternate vortex street was established in the wake.

In the current study, it is found that at $\alpha=8^\circ$, a low amplitude vortex shedding is observed by investigating the Strouhal number based on the amplitude of the Fast Fourier Transform of the

instantaneous lift coefficient. However, in the meantime, the alternating vortices are observed behind the airfoil at the wake (Figure 19). The Strouhal number is defined by Eq. (4).

$$St = \frac{fc}{U_{inf}} \quad (4)$$

where f is the frequency corresponding to the maximum amplitude of the amplitude spectrum of the instantaneous lift coefficient.

The amplitude spectrum of lift coefficient at 8° , shows a peak at a Strouhal number of 0.876 but at very low amplitude values. The same Strouhal number is obtained from the amplitude spectrum of drag coefficient.

It is observed that the moment coefficient at $c/4$ location becomes unsteady for $\alpha=9^\circ$. Similarly, vortex shedding mechanism effect is visible in lift and drag coefficients for this angle of attack. For lower angles of attack, there is no vortex shedding from the airfoil surface and the aerodynamic coefficients converges to steady state values after the computational start-up effect of the flowfield. This transition lead to the sinusoidal oscillation of aerodynamic coefficients. The mean values and amplitudes of the parameters are increasing with the increase of the angle of attack above $\alpha=9^\circ$.

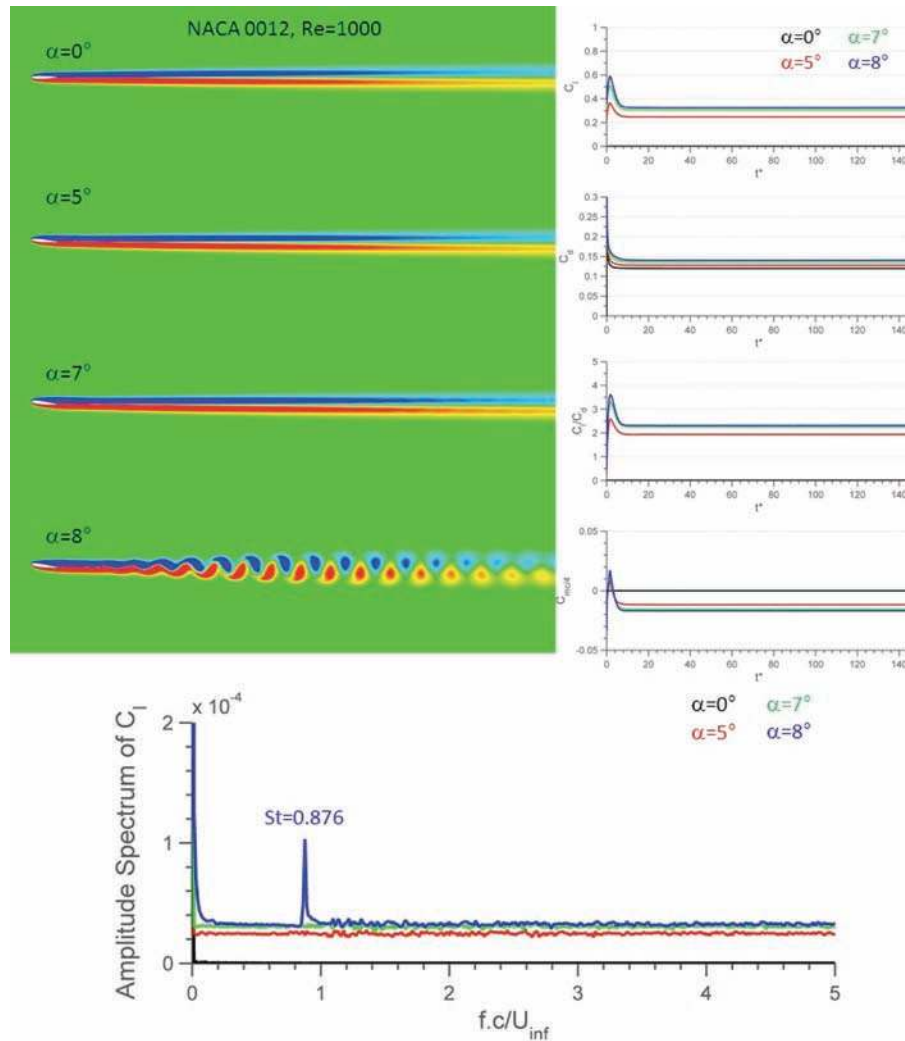


Figure 19. Vortex pattern, aerodynamic coefficients and Amplitude spectrum of C_l for NACA 0012 at $\alpha=0^\circ, 5^\circ, 7^\circ$ and 8°

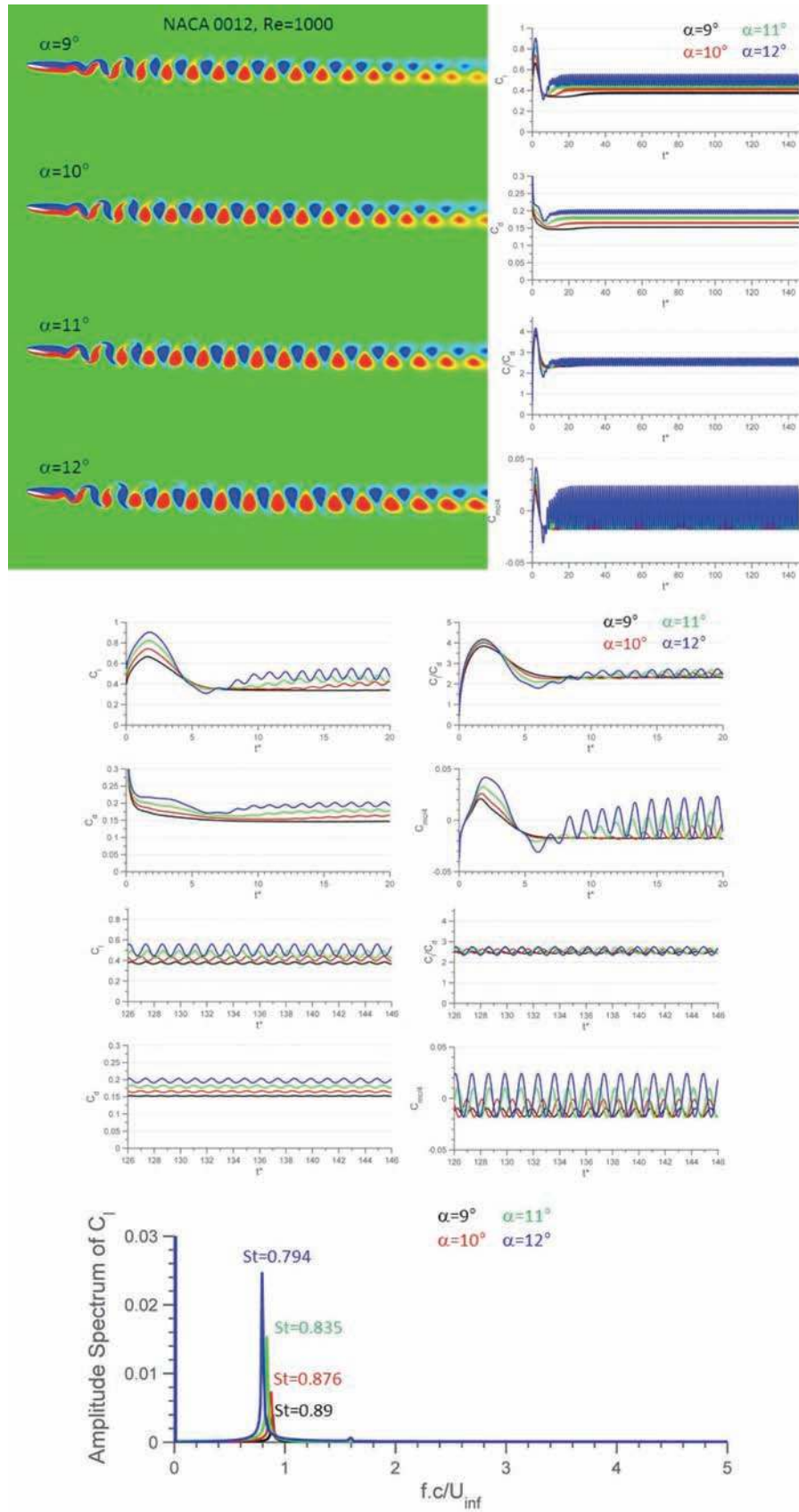


Figure 20. Vortex pattern, aerodynamic coefficients and Amplitude spectrum of C_l for NACA 0012 at $\alpha=9^\circ$, 10° , 11° and 12°

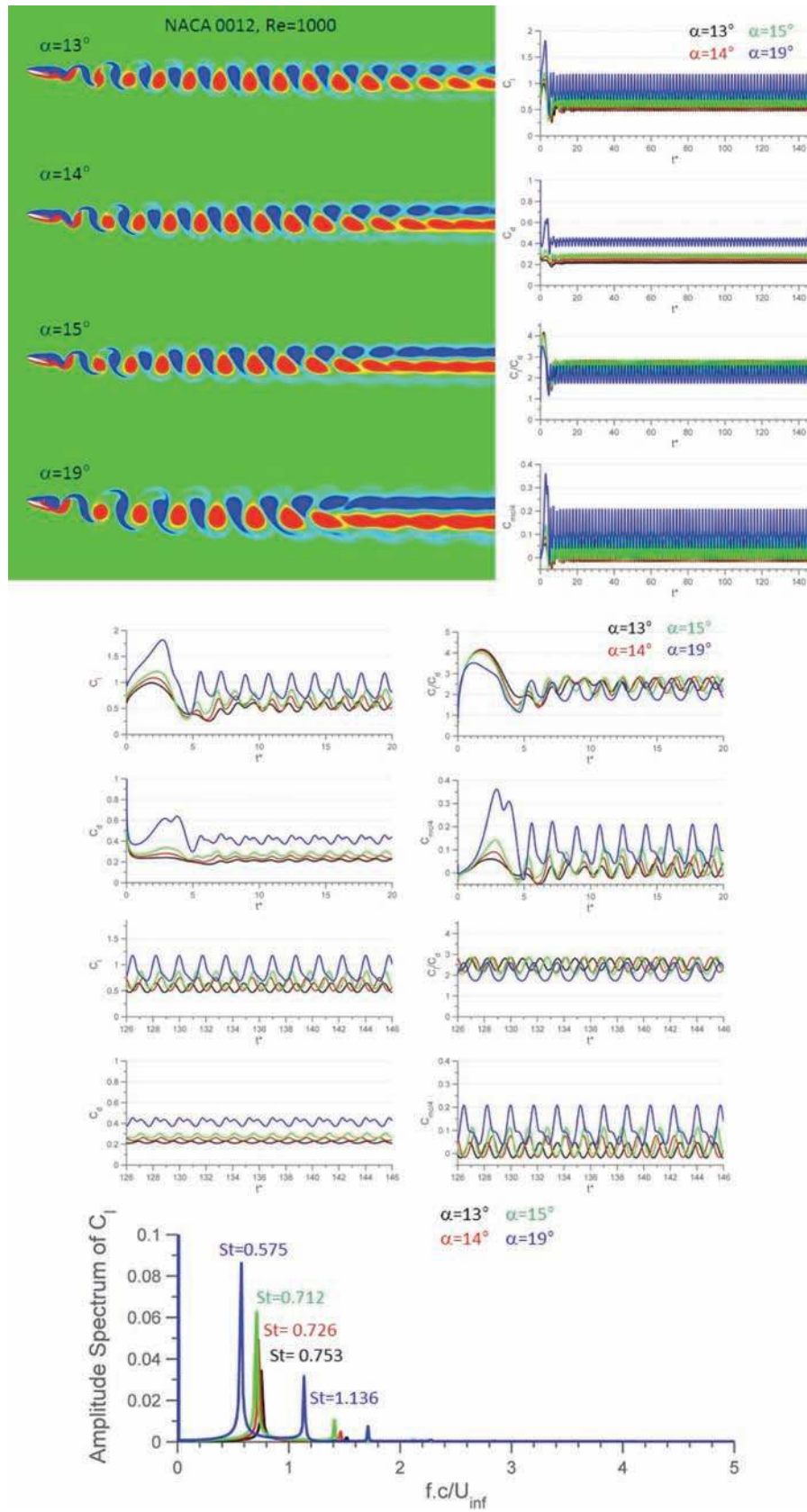


Figure 21. Vortex pattern, aerodynamic coefficients and Amplitude spectrum of C_l for NACA 0012 at $\alpha=13^\circ$, 14° , 15° and 19°

At $\alpha=15^\circ$, a laminar separation bubble is formed at $t^*=0.7$ on the first half of the airfoil. At $t^*=1.5$, the separation bubble covers almost all the upper surface of the airfoil. At $t^*=3$, the flow is fully detached from the upper surface of the airfoil. After this time, a new trailing edge vortex is formed.

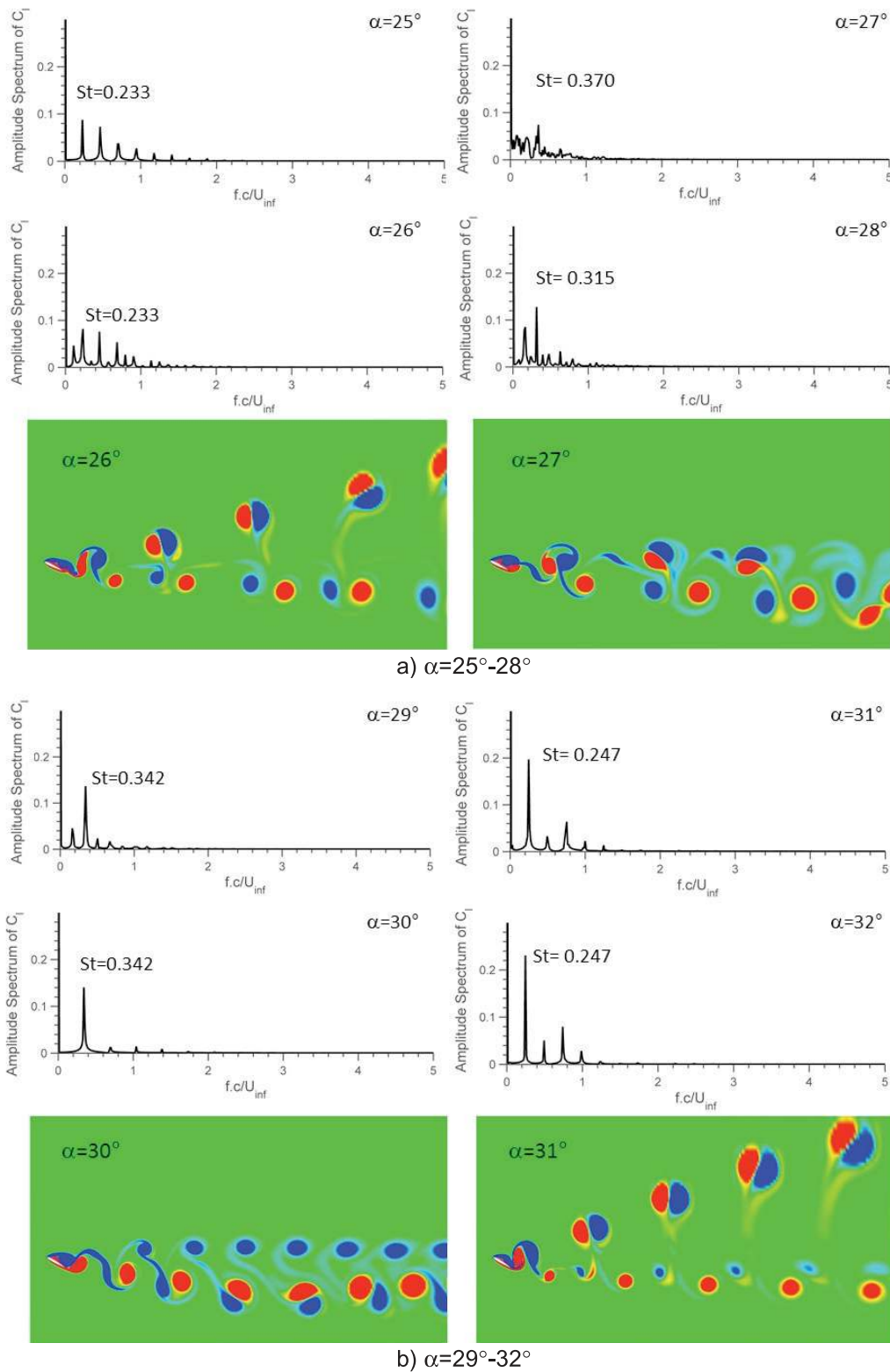
Vortex pattern change for $\alpha=19^\circ$. It is observed that C_l/C_d values for $\alpha=19^\circ$ diminishes compared to lower angles of attack. The vortex pattern is alternating and in the form of a single branch from 19° to 22° . A vortex splitting is observed at 23° angles of attack. This two branch of vortex structure can be visualized until $\alpha=41^\circ$ for the current study. The vortex shedding of 50° angle of attack and higher angles of attack becomes ones more alternating with strong vortex structures growing a while close to the airfoil by forming a bigger vortex structure before shedding to the wake.

In the discussion of mean aerodynamic coefficients, it was stated that the mean drag coefficient has a local maximum at $\alpha=26^\circ$ and then a very small decrease in drag coefficient was observed different than overall trend of the drag coefficient which has tendency to increase as angle of attack increases until $\alpha=90^\circ$. From the amplitude spectrum of C_l , It is observed that the amplitude spectrum of $\alpha=27^\circ$ reveals a dense spectrum of frequencies as is also observed by Khalid et al. [19]. The spectrum which was ordered in amplitude at $\alpha=25^\circ$, shows period doubling at $\alpha=26^\circ$ and then chaotic vortex shedding frequencies at $\alpha=27^\circ$ (Figure 22a). At $\alpha=29^\circ$, the amplitude spectrum of C_l becomes smooth and vortex shedding pattern turns out to be more ordered (Figure 22b).

It was also discussed that there was a sudden jump in aerodynamic coefficients between 30° and 31° . The instantaneous vortex pattern is observed to be changed between these two angles as can be observed from Figure 22b. It is also known that as the width of the wake increases, the drag coefficient increases. The wake with is increased from 30° to 31° result a sharp increase in the drag. The time-averaged streamline pattern close to the airfoil was also observed to be changed as seen in Figure 9. The thickness of the vortex pattern on the upper surface of the airfoil was decreased and vortex pattern was changed. Trailing edge vortices generated also causes this instantaneous vortex pattern distribution dissimilar to each other.

In the interval of $31^\circ \leq \alpha \leq 39^\circ$ vortex shedding pattern is the same and this also results a constant Strouhal number of about 0.25. At angles of attack higher than 60° , the vortex pattern resembles to bluff body vortex shedding pattern as can be seen also from Figure 23.

It is noted by Huang et al. [26] that between $\alpha=17^\circ$ - 60° , the boundary layer separating from the leading edge formed vortices, which grew in size as advected downstream. Above $\alpha>60^\circ$, vortices were shed from the two edges in an alternate fashion. In the current study, it is found that the frequency shedding varies very slowly for $\alpha \geq 40^\circ$ from about $St=0.23$ to $St=0.123$ for $\alpha=70^\circ$, then stays constant for $\alpha=80^\circ$ and $\alpha=90^\circ$ at this Strouhal number. This constant region of frequency shedding looks similar to bluff body vortex shedding phenomena as it is observed for example flows around circular or square cylinders [34-39].

Figure 22. Vortex pattern and Amplitude spectrum for NACA 0012 at $\alpha=25^\circ-32^\circ$

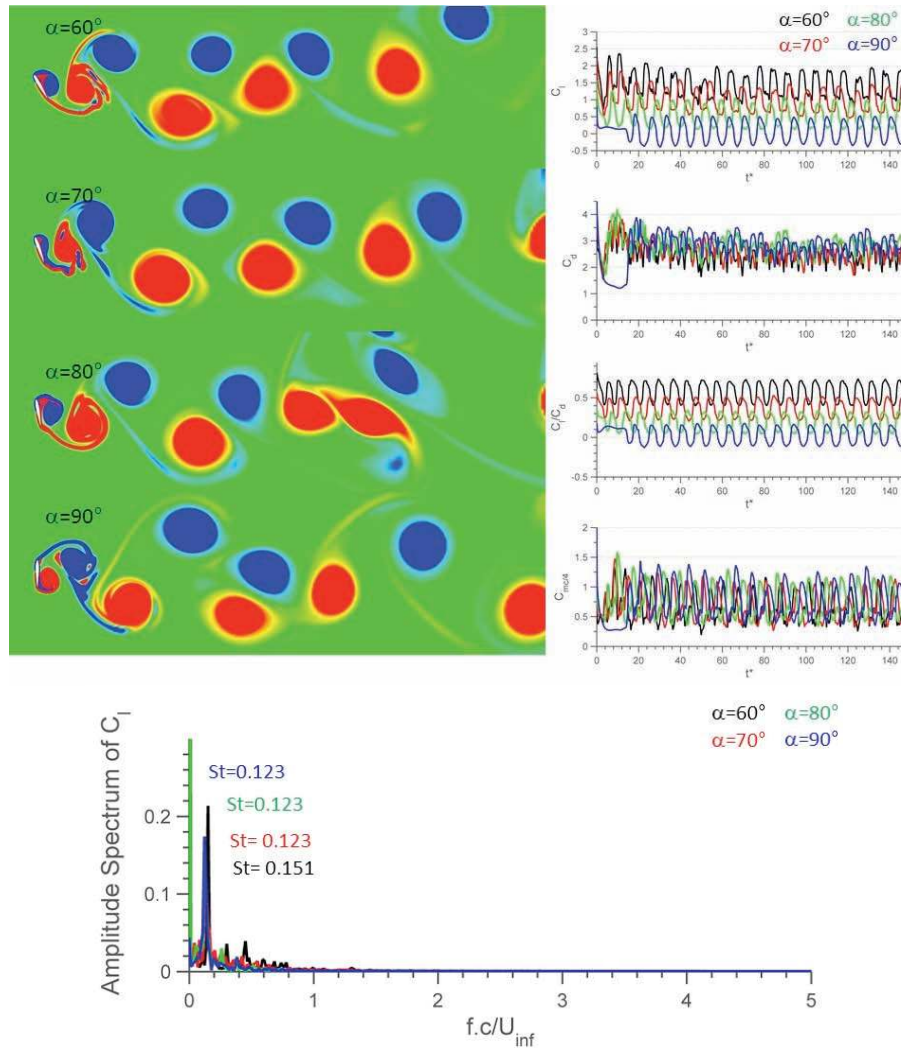


Figure 23. Vortex pattern, aerodynamic coefficients and Amplitude spectrum for NACA 0012 at $\alpha=60^\circ$, 70° , 80° and 90°

3.3 Strouhal number

Amplitude spectrum, calculated using FFT algorithm, was determined based on the lift coefficient. The results are obtained between $73 < t^* < 146$ time interval in order to avoid initial computational starting effects. Strouhal number is obtained from the amplitude spectrum of C_L . The frequency is selected to be the maximum amplitude in the spectrum. This frequency peak is due to vortex shedding from the airfoil. Frequency (f) resolution in the spectral analysis was 0.02 Hz. The results are presented with respect to non-dimensional frequency fc/U_{inf} . The results are compared with Strouhal numbers obtained from the lift spectrum by the numerical solution of Mittal et al [21] for $\alpha=10^\circ$ and DNS result of Hoarau et al. [20] for $\alpha=20^\circ$ at $Re=1000$. In addition, the solution is also compared at higher angles of attack with the results of Mahbub Alam et al. [15] at $Re=5300$ and $Re=10500$. The trendline of Strouhal number with respect to angle of attack given in Figure 24 seems to be comparable with the results in literature at low Reynolds numbers.

The Strouhal number can also be defined with respect to projected chord length ($c \cdot \sin \alpha$). This calculation of Strouhal number based on projected chord is also shown in Figure 24b. The shedding frequency of the starting critical angle of attack ($\alpha=8^\circ$) is found to be 0.122 which is almost equal to the Strouhal number for 90° angle of attack. Similarly, for $\alpha=31^\circ$, a value of 0.127 is obtained. Strouhal number of 0.12 based on projected chord is also obtained by Taira and Colonius [32] for wings at low aspect ratio having periodic vortex shedding. They conclude that when the flow is periodic, the dominant features are the shedding of the leading- and trailing-edge vortices at a constant frequency of

0.12 [32, 33]. The Strouhal number based on the projected chord for all angles of attack investigated is found to be between 0.1-0.2.

There is no a characteristic frequency observed below 8° (as can be seen also from the amplitude spectrum shown in Figure 19). The maximum Strouhal number is obtained at $\alpha=9^\circ$ with the normalized vortex shedding frequency $St (=f c/U_{inf})$ equal to 0.89 (Figure 24). After this angle of attack, Strouhal number drops rapidly with a until $\alpha=23^\circ$ where it reaches a value of $St=0.45$. A slight increase is observed at $\alpha=24^\circ$. Then, the peak of the spectrum amplitude shifts to a lower frequency of $St=0.23$ for $\alpha=25^\circ$ (about the half of the previous angle of attack's Strouhal number).

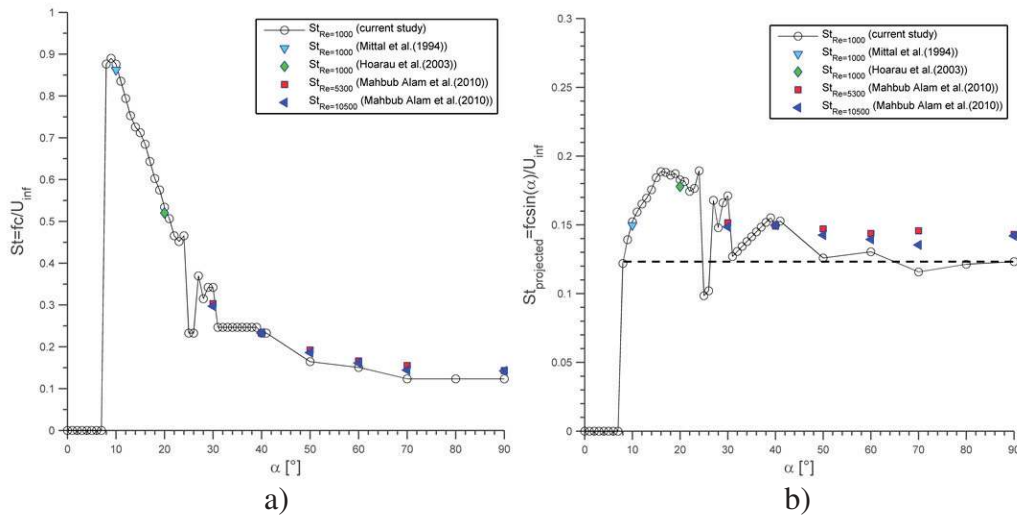


Figure 24. Strouhal number based on amplitude spectrum of C_1

A local peak is observed at $\alpha=27^\circ$ with $St=0.37$, then the frequency decreases and increases slightly around $St=0.32$ - 0.34 until $\alpha=30^\circ$. There is a constant vortex shedding interval between $31^\circ \leq \alpha \leq 39^\circ$ where Strouhal number is about 0.25. Thereafter, the frequency shedding varies very slowly for $\alpha \geq 40^\circ$ from $St=0.23$ (for $\alpha=40^\circ$ and 41°) to $St=0.123$ for $\alpha=70^\circ$. It is denoted that the rapid drop in St is associated with a rapid retreat in the vortex formation length and a growth in the wake width and wavelength of K-H (Kelvin-Helmholtz) vortices [15]. Then, the Strouhal number is fixed to 0.123 for $\alpha=80^\circ$ and $\alpha=90^\circ$. For angles of attack higher than 70° , the flow behind the airfoil resembles to a bluff body.

The same numerical simulations are also performed for a thinner airfoil (NACA0002) and interestingly, it is noted that same Strouhal number of 0.123 is obtained at these angle of attack and Reynolds number of 1000. It is noted that the shedding frequency for bluff bodies is proportional to the freestream velocity, and the value of the Strouhal number remains constant if the width between shear layers remains unchanged [35].

It is concluded that for larger angles of attack, the frequency becomes smaller which implies that the shedding period of Karman vortices are longer. In literature, it is also denoted that as the shedding period increases with angle of attack, the more K-H vortices are amalgamated to form one Karman vortex [15, 36].

It should also be noted that in a previous study carried out by the author [34] with time resolved PIV measurements at a rate of 1kHz around a square cylinder with $Re=4900$, the Strouhal number based on the C_1 value is found to be around 0.128 which was in agreement with Bearman and Obasaju [39].

It is obvious that as width of the wake increases, the drag coefficient increases. However, inversely, it is observed that Strouhal number is decreased with the increase of the wake width. Similar trend is observed for bluff bodies as circular cylinders who have lower Strouhal numbers with the increase of the wake width [37] since the bluffer body tends to diverge the flow more, to create a wider wake, and to have larger drag.

4. CONCLUSION

The current study investigated the unsteady flowfield around a symmetric airfoil, namely NACA 0012, for the angle of attack ranges of 0° to 90° . The results are obtained with 1° increments from $\alpha=0^\circ$ to $\alpha=41^\circ$ and with 10° increments from $\alpha=40^\circ$ until 90° . A good comparison is obtained with results in literature. The effect of angle of attack to wake pattern and instantaneous and mean aerodynamic coefficients are discussed.

Spectral analysis is performed for angles of attack ranging from 0 to 90 degrees. It is presented that amplitude spectrum of C_l coefficient start to shows a peak at 8° for NACA 0012 and the aerodynamic forces presents oscillatory behavior afterwards. The peak Strouhal number value for the vortex shedding is obtained at $\alpha=9^\circ$. There is no a characteristic frequency observed below 8° .

Stall angle is observed to be at about $\alpha=26^\circ$ by considering mean values of the lift coefficients. Higher than 8° , the amplitude of lift coefficient is observed to increase until it reaches its peak value at $\alpha=27^\circ$. Beyond the stall angle of attack, mean C_l displays a maximum value at around $\alpha=40^\circ$. It is also noted that the lift curve slope $C_{l\alpha}$ is equal to π at $\alpha=0^\circ$ which is half of the linearized lift curve slope of 2π . Then, the curve slope decreases until $\alpha=8^\circ$ where a sudden increase of lift curve slope is observed afterwards. It should be noted that the lift curve slope is function of airfoil thickness [16]. $C_{m\alpha}$ is found to be negative around 0° .

Strouhal number is found to be constant between $31^\circ \leq \alpha \leq 39^\circ$ where Strouhal number is about 0.25. Strouhal number based of lift coefficient is found to be fixed above 70° to about 0.123. The Strouhal number based on the projected chord ($c \cdot \sin \alpha$) reveals approximately same values for $\alpha=8^\circ$ ($St_{\text{projected}}=0.122$), $\alpha=31^\circ$ ($St_{\text{projected}}=0.127$) and $\alpha=90^\circ$ ($St_{\text{projected}}=0.123$). The Strouhal number based on the projected chord for all angles of attack investigated is found to be between 0.1-0.2.

A vortex splitting is observed at 23° angle of attack. The vortex splitting pattern can be observed until $\alpha=41^\circ$ for the current study. As width of the wake increases, the drag coefficient increases. The vortex pattern for $\alpha \geq 50^\circ$ shows that vortices are amalgamated with time before it is shed to the wake as a single Karman Vortex.

ACKNOWLEDGEMENTS

This work is supported TUBITAK 213M327 project. The financial support from Turkish Academy of Science-Young Scientific Award (TUBA GEBIP) is gratefully acknowledged by the author.

REFERENCES

- [1] Shyy, W., Lian, Y., Tang, J., Viieru, D. and Liu, H., *Aerodynamics of Low Reynolds Number Flyers*, New York: Cambridge Univ. Press, 2008.
- [2] Mueller, T. J. and Delaurier, J. D., *Fixed and Flapping Wing Aerodynamics for Micro Air Vehicle Applications*, Reston, Virginia: AIAA, 2001.
- [3] Kang, C. K. and Shyy, W., Scaling law and enhancement of lift generation of an insect-size hovering flexible wing, *J R Soc Interface*, 10: 20130361, 2013
- [4] Windte, J., Radespiel, R., Scholz, U. and Eisfeld, B., *RANS Simulation of the Transitional Flow Around Airfoils at Low Reynolds Numbers for Steady and Unsteady Onset Conditions*, Proc. Specialists Meeting on Enhancement of NATO Military Flight Vehicle Performance by Management of Interacting Boundary Layer Transition and Separation, Prague, Czech Republic, RTO-MP-AVT-111-P-03, 2004.
- [5] Ol, M., McAuliffe, B. R., Hanff, E. S., Scholz, U. and Kaehler, C., *Comparison of Laminar Separation Bubble Measurements on a Low Reynolds Number Airfoil in Three Facilities*, AIAA Paper, 2005, 5149
- [6] Platzer, M. F., Jones, K. D., Young, J. and Lai, J. C. S., Flapping-Wing Aerodynamics: Progress and Challenges, *AIAA Journal*, 2008, 46 (9), 2136–2149
- [7] Kurtulus, D. F., Farcy, A. and Alemdaroglu, N. *Unsteady Aerodynamics of Flapping Airfoil in Hovering Flight at Low Reynolds Numbers*, AIAA Paper, 2005, 1356
- [8] Ohmi K., Coutanceau, M., Loc T. P. and Dulieu A., Vortex formation around an oscillating and translating airfoil at large incidences, *J. Fluid Mech*, 1990, 211, 37-60
- [9] Ohmi K., Coutanceau, M., Daube, O. and Loc, T. P., Further experiments on vortex formation around an oscillating and translating airfoil at large incidences, *J. Fluid Mech*, 1991, 225, 607-630

- [10] Kurtulus, D.F., David, L., Farcy, A. and Alemdaroglu, N., Aerodynamic Characteristics of Flapping Motion in Hover. *Experiments in Fluids*, 2008, 44, 23–36
- [11] Ol, M.V., Eldredge J. D., Wang C. High-Amplitude Pitch of a Flat Plate: an Abstraction of Perching and Flapping, *International Journal of Micro Air Vehicles*, 2009, 1(3), 203-216
- [12] Krone T.P, Baik Y. S., Rausch J. M., Bernal L. P. Aerodynamics of a Successful Perching Maneuver, *AIAA Paper*, 2011, 218
- [13] Gopinath A. K. and Jameson, A., Application of the Time Spectral Method to Periodic Unsteady Vortex Shedding, *AIAA Paper*, 2006, 0449
- [14] Shyy, W., Aono, H., Kang, C. K. and Liu, H., *An introduction to Flapping Wing Aerodynamics*, Cambridge University Press, 2013
- [15] Mahbub Alam , M., Zhou, Y., Yang, H. X., Guo, H. and Mi, J. The ultra-low Reynolds number airfoil wake, *Exp Fluids*, 2010, 48, 81–103
- [16] Kunz, P. and Kroo, I., Analysis and Design of Airfoils for Use at Ultra-Low Reynolds Numbers, *Proc. AIAA Fixed, flapping and rotating wing aerodynamics at very low Reynolds numbers conference*, edited by T. J. Mueller, Notre Dame, June 5-7, 2000, pp. 35-60
- [17] Mateescu, D and Abdo, M., Analysis of flows past airfoils at very low Reynolds numbers, *Proc. IMechE Part G: J. Aerospace Engineering*, 224, 757-775
- [18] Ahuja S. and Rowley C. W., Feedback control of unstable steady states of flow past a flat plate using reduced-order estimators, *J. Fluid Mech.*, 2010, 645, 447-478
- [19] Hoarau, Y., Braza, M., Ventikos, Y., Faghani, D. and Tzabiras, G., Organized modes and the three-dimensional transition to turbulence in the incompressible flow around a NACA0012 wing, *J. Fluid Mech.*, 2003, 496, 63–72.
- [20] Hoarau, Y., Braza, M., Ventikos, Y. and Faghani, D., First Stages of the Transition to Turbulence and Control in the Incompressible Detached Flow around NACA0012 Wing, *International Journal of Heat and Fluid Flow*, 2006, 27, 878-886.
- [21] Mittal, S. and Tezduyar, T.E., Massively parallel finite element computation of incompressible flows involving fluid-body interactions, *Computer Methods in Applied Mechanics and Engineering*, 112, 1994, 253-282
- [22] Liu, Y., Li, K., Zhang, J., Wang, H. and Liu, L., Numerical bifurcation analysis of static stall of airfoil and dynamic stall under unsteady perturbation. *Commun Nonlinear Sci Numer Simulat*, 17, 2012, 3427–3434
- [23] Khalid M. S. U. and Akhtar I., *Characteristics of flow past a symmetric airfoil at low Reynolds Number: A nonlinear perspective*, Proceedings of the ASME 2012 International Mechanical Engineering Congress & Exposition IMECE2012, IMECE2012-87389, November 9-15, 2012, Houston, Texas, USA
- [24] Suzuki T., Ji H. and Yamamoto F., Unsteady PTV velocity field past an airfoil solved with DNS: Part 1. Algorithm of hybrid simulation and hybrid velocity field at $Re = 10^3$, *Exp Fluids*, 2009, 47, 957–976
- [25] Suzuki T., Sanse A., Mizushima T. and Yamamoto F., Unsteady PTV velocity field past an airfoil solved with DNS: Part 2. Validation and application at Reynolds numbers up to $Re = 10^4$, *Exp Fluids*, 2009, 47, 977–994
- [26] Huang, R.F., Wu, J.Y., Jeng, J.H. and Chen, R.C., Surface flow and vortex shedding of an impulsively started wing, *J. Fluid Mech.*, 2001, 441, 265-292
- [27] ANSYS Fluent Userguide, ANSYS Inc.
- [28] NACA Technical Memorandum 4741, *Computer Program To Obtain Ordinates for NACA Airfoils*, December 1996
- [29] Abbott, I. H., and von Doenhoff, A. E., *Theory of Wing Sections*, Dover, New York, 1959, ISBN 0-486-60586-8
- [30] Katz J. and Plotkin A., *Low Speed Aerodynamics- From Wing Theory to Panel Methods*, McGraw Hill, International Edition, 1991.
- [31] McAlister K.W. and Carr L.W., *Water-Tunnel Experiments on an Oscillating Airfoil at $Re=21000$* , NASA TM 78446, 1978

- [32] Taira, K., and Colonius, T., Three-Dimensional Separated Flows around Low-Aspect-Ratio Flat Plates, *Journal of Fluid Mechanics*, 2009, 623, 187–207.
- [33] Taira, K., Rowley C. W., Colonius, T., Williams, D. R., Lift Enhancement for Low-Aspect-Ratio Wings with Periodic Excitation, *AIAA Journal*, 2000, 48 (8), 1785-1790
- [34] Kurtulus D. F., Scarano F. and David L., Unsteady aerodynamic forces estimation on a square cylinder by TR-PIV. *Experiments in Fluids*, 2007, 42 (2), 185-196
- [35] Zdravkovich, M. M., Different Modes of vortex shedding: an overview, *Journal of Fluids and Structures*, 1996, 10, 427 – 437
- [36] Yarusevych S., Sullivan P. E., Kawall J. G., On vortex shedding from an airfoil in low-Reynolds-number flows, *J. Fluid Mech.*, 2009, 632, 245-271
- [37] Roshko A., *On the drag and shedding Frequency of two dimensional bluff bodies*, NACA Technical Note 3169. 1954
- [38] Bearman P. W., *On Vortex Street Wakes*, NPL Aero Report 1199, A.R.C 28 143, 1966
- [39] Bearman, P.W. and Obasaju, E. D., An experimental study of pressure fluctuations on fixed and oscillating square-section cylinders. *J Fluid Mech*, 1982, 119, 297–321